Contents lists available at SciVerse ScienceDirect

CIRP Annals Manufacturing Technology

Journal homepage: www.elsevier.com/locate/cirp

Printability assessment and modelling for process optimization of 3D Aerosol Jet® printed high aspect ratio microstructures

Elisabetta Ceretti (2)[a*#], Mohit Sharma[b#], Eleonora Ferraris (2)[c], Paola Serena Ginestra[a], Miriam Seiti[a,c]

[a] *Department of Mechanical and Industrial Engineering, University of Brescia, Brescia, 25123, Italy*
[b] *Department of Electrical Engineering, ESAT-STADIUS KU Leuven, Leuven, 3000, Belgium*
[c] *Department of Mechanical Engineering, KU Leuven, Sint Katelijne Waver, 2860, Belgium*
#Authors contributed equally

The printability assessment of high-aspect-ratio structures in additive manufacturing is critical for ensuring dimensional accuracy and functional properties. This study proposes a method to evaluate print quality by quantifying metrics, including accuracy, shape fidelity and line edge quality, using advanced imaging and predictive analysis. A printability index is developed to relate these metrics to process parameters, here applied to Aerosol Jet® Printing. By validating structures' quality and optimizing parameters, the index effectively improves process stability, reduces defects, and enhances structural precision. This approach provides a robust tool for process optimization, ensuring consistent results in complex high-aspect-ratio designs, further advancing printing scalability and reproducibility.

Additive Manufacturing; Optimization; High-Aspect-Ratio.

1. Introduction

High-aspect-ratio (HAR) microstructures (*e.g.*, micropillars, pins, arrays, etc.) are crucial in many advanced applications because their geometry allows for precise control over physical and functional properties [1]. Mechanically, their thin and tall dimensions enable unique behaviours, such as enhanced flexibility, high stiffness, or tailored deformation, which are fundamental in microscale applications [2]. Electrically, they facilitate interconnects in microelectronics, improving performance by reducing signal loss and crosstalk in miniaturized circuits. They also improve the surface area, thus providing higher thermal conductivity or charge transfer, like in thermoelectric interfaces. Finally, the surface properties of HAR designs, including regulated porosity or increased roughness, have utility in domains like fluid dynamics, adhesion, and optical performance. As a result, they are crucial in various applications, including energy storage, photonics, medical devices, (bio)sensors, and microfluidics [3].

To produce high-precision three dimensional (3D) HAR microstructures, it is essential to select specific techniques that offer high resolution and process control over geometrical accuracy and material properties [4]. Processes, as micromachining, micro-milling, laser beam, hot embossing, microinjection moulding are generally reliable. Technologies like soft lithography, photolithography and two-photon polymerization, are also promising, yet often very complicated and composed by numerous steps [5], [6].

Additive manufacturing (AM) is an emerging domain to produce customized and personalized HAR microstructures, despite the technical limits at a microscale resolution [7]. This complicates the production of straight HAR features and smooth surfaces, critical for functional performances. In AM, VAT-polymerization technologies (such as micro-stereolithography and digital light printing), material extrusion, ink-jet printing and Aerosol Jet® Printing (AJ®P), can currently offer high precision and scalability for HAR microstructures [8] but it is quite rare to achieve a robust process control [9], [10]. Advanced support strategies and post-processing treatments can also be applied to enhance the precision and stability of the printed structures. However, supports are difficult to remove from HAR microstructures, and post-processing techniques, like curing or sintering, may cause thermal distortions, affecting the intended geometry.

In this context, the main challenge is the numerical and metrological assessment of HAR microstructure quality. HAR designs indeed frequently encounter problems such as distortion, collapse, or precision failure due to their high, thin and microscale shape. Due to these factors, optical measurements of HAR microstructures are difficult to obtain and often lack a direct association to a numerical assessment, especially in relation to the process parameters. This challenge increases with the increase of the desired Aspect Ratio (AR) of the feature in question. In addition, limited imaging techniques exist for assessing micro-HAR metrics [11]. These aspects are compounded by the need of specialized materials and methods to ensure printability, often requiring extensive process optimization and complex measuring equipment [12].

Therefore, the identification of a reliable and up-to-date Printability Index (PI) to assess the quality of HAR 3D printed microstructures is crucial and complex due to the variety of parameters that influence the results [13]. The quality of a printed structure depends on geometrical accuracy, but also on other properties, such as material cohesion, shape fidelity and absence of defects, influenced by material state, process design and operating limits of each AM technique. A robust mathematical model for evaluating these properties by integrating metrics, can be used to optimize process parameters, thereby reducing trial-and-error experimental time.

This research presents and compares two novel PIs, the arithmetic mean index Ψ_A [#] and the geometric mean index Ψ_G [#],

due to the lack of a versatile and comprehensive index for evaluating the manufacturing quality of microstructures. The two PIs consist of an innovative combination of four selected sub-indexes assessing ideal geometrical metrics, here applied to the 3D printing of HAR micropillars. 3D AJ®P is selected in this work as innovative and highly potential additive manufacturing techniques for producing HAR 3D microstructures. AJ®P was initially developed for planar electronics, due to its ability to generate an aerosol jet from liquid inks and deposit it on *free-form* substrates with a resolution as fine as 15 µm. However, AJ®P recently shown its potential as 3D micro-AM technique for the production of pillars or lattice structures [14]. The two main AJ®P parameters are the carrier gas flow (*CGF* = [0-45] sccm), which carries the aerosol mist, and the sheath gas flow (*SGF* = [0-200] sccm), which focuses the mist into an aerosol jet, as depicted in Figure 1a. In this study, the *CGF* and the focusing ratio (*Rf*, *i.e.*, the ratio between *SGF* and *CGF*) are investigated to assess the printability of HAR AJ® printed micropillars, using the PIs as final outcomes. A mathematical model is then developed using least squares-based sparse parameterization, implemented with least absolute shrinkage and selection operator (LASSO) regression technique, to establish the direct relationship between the process parameters and the PIs. The model is finally validated and optimal parameters are used to successfully AJ® print high quality 3D HAR micropillars. This method allows the efficient selection of relevant process parameters and quantifies their influence on the PIs, while minimizing the overfitting in the mathematical model.

2. Materials and Methods

The methodological flow chart used in this study is reported in Figure 1b. The HAR microstructures are fabricated and their quality inspected by advanced image analysis. The PI indexes are then calculated and a mathematical model for process optimization is generated and validated for predictive analysis. In the next paragraphs, each step is thoroughly explained.

2.1. Materials, printing process and characterization

A Poly(3,4-ethylenedioxythiophene) polystyrene sulfonate (PEDOT:PSS)-based ink was used as 3D AJ®P material. The ink was previously demonstrated by the authors for 3D AJ®P applied in bioelectronics [14]. An Optomec 300s machine (Optomec, USA) in the ultrasonic mode was used as 3D AJ®P print system. Nitrogen (N_2) was used for both *CGF* and *SGF*. A nozzle diameter, $\emptyset$ = 150 µm, a stand-off distance, z = 3 mm, a platen temperature, T = 80 °C, and a total number of layers, n = 25 were selected. The ink was AJ printed on glass slides (VWR Superfrost®) as an array of 6x4 circles, each with a diameter of $\emptyset$ = 50 µm and centre-to-centre distance of 150 µm. The calculation of the two PIs was based on the target process parameters within the Design of Experiment (DOE) window: *Rf* = (1,3) and *CGF* = (20,30,40) sccm, as shown in Table 1. Generally, a *CGF* ≥ 20 sccm and a *Rf* ≥ 1 are required for a stable aerosol flow and for a converged aerosol jet, respectively. Each condition was repeated three times. After printing, the pillars were thermally annealed at 140 °C for 1 hour. Micropillars images were acquired using an optical microscope (Hirox KH8700, CZ) and analysed with the software Image J. For each output, the mean (μ) [µm] and standard deviation (σ) [µm], denoted as $\mu \pm \sigma$, were calculated and analysed.

2.2. HAR Printability Indexes and Model

The calculation of the two PIs, Ψ_A [#] and Ψ_G [#], was carried out considering four sub-indexes: i) the uniformity index i_u [#], ii) the

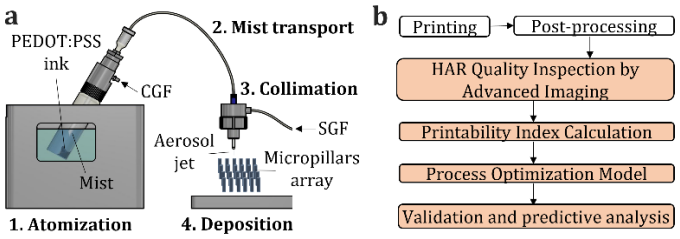

Figure 1. Printability assessment and 3D AJ®P process: a) Working principle for 3D AJ®P and b) PI and model methodology flow chart.

Table 1. 3D AJ®P parameters used in the experimental test.

3D AJ®P parameters			
Design of experiment	**Values**		
Carrier gas flow, *CGF* [sccm]	20	30	40
Focusing Ratio, *Rf* [#] (SGFs)	1 (20,30,40)		3 (60,90,120)
Repetition [#]	3		
Output	Printability Indexes [#]		

AR index i_{AR} [#], iii) the bending angle index i_α [#], and the iv) Line Edge Roughness (LER) index i_{LER} [#]. Every index is a continuous variable ranging from 0 to 1, with 0 representing the ideal condition, here referred to a perfect cylinder, as shown in Figure 2a. Equation (1) describes i_u as the average value of the average among the normalized ratios between each diameters difference measured at three different points, namely top ($\emptyset_1$), middle ($\emptyset_2$), and base ($\emptyset_3$) diameter:

$$i_u = \frac{1}{3} \sum_{i,j \in {}^3C_2} \left| \frac{(\emptyset_i - \emptyset_j)}{\emptyset_\mu} \right|, \quad 0 \le i_u \le 1 \tag{1}$$

where ${}^3C_2$ represents the total number of (i,j) combinations of two selected diameters out of a total of three and the $\emptyset_\mu$ is the average of the three diameter values. Equation (2) defines i_{AR} as the absolute ratio between the maximum value between the top and base diameter over the height (essentially the inverse of the AR). This implies that the processing conditions are fine-tuned to achieve a minimum i_{AR}, which in turn results in a maximum AR.

$$i_{\mathrm{AR}} = \left| \frac{max\,(\emptyset_1, \emptyset_3)}{h} \right|, 0 \le i_{AR} \le 1 \tag{2}$$

Equation (3) characterizes i_α as the absolute value of the normalized difference between an angle of $\frac{\pi}{2}$ and the bending angle α.

$$i_\alpha = \left| \frac{\left(\frac{\pi}{2} - \alpha\right)}{\frac{\pi}{2}} \right|, \quad 0 \le i_\alpha \le 1 \tag{3}$$

The evaluation of the line edge quality also plays a crucial role in assessing the overall printability of the pillars. In general, line edge quality characterizes the width fluctuations of a feature along its length. In literature, the so-called line edge roughness (LER) is commonly employed for characterizing edge surface quality [15]. We focused on LER as a parameter to assess the surface quality as an edge shape deviation because in our specific application, any form of edge shape deviation, be it circular or non-circular, is equally undesirable. Due to the complexity of obtaining a complete 3D mapping of the surface of a microfeature, it is common practice to measure the surface profile in the 2D image (Figure 2a). The LER is mathematically defined as three times the standard deviation of the digression of each line edge l^{th}, from a straight line that provides the best fit for that edge (Equation 4).

$$\gamma_l^{LER} = 3. \sqrt{\frac{1}{N_l} \sum_{j=1}^{N_l} \left(\Delta\vartheta_{lj} - \mu_l\right)^2} \tag{4}$$

where N_l represents the total number of observed points on l^{th} edge, $\Delta\vartheta_{lj}$ denotes the residual of the point j on the l^{th} edge from the best-fitted straight line for the l^{th} edge, and μ_l represents the average of the edge residuals for the l^{th} edge, as in Equation 5:

$$\mu_l = \frac{1}{N_l}\sum_{j=1}^{N_l}\Delta\vartheta_{lj} \quad (5)$$

The mean LER (μ_{LER}) is computed in Equation 6 to quantify the overall LER of the number of printed pillars (L) with same printing parameters, with $L \geq 5$:

$$\mu_{LER} = \frac{1}{L}\sum_{l=1}^{L}\gamma_l^{LER} \quad (6)$$

Finally, the LER index (i_{LER}) is calculated in Equation 7 as the mean of the each normalized μ_{LER} on the maximum mean value of the total data set:

$$i_{LER} = \frac{\mu_{LER_n}}{\max(\mu_{LER})} \quad (7)$$

The first PI Ψ_A is formulated by considering the mean values of all sub-indexes, that correspond to the arithmetic mean (AM), as in Equation 8:

$$\Psi_A = AM(i_u, i_{AR}, i_\alpha, i_{LER}) \quad (8)$$

The AM serves as a measure to evaluate the degree of resemblance between the printed pillars and the idealized shape, which is here referred to a perfect cylinder.

For a complete analysis, a second index Ψ_G is considered using the geometric mean (GM), as in Equation 9:

$$\Psi_G = GM(i_u, i_{AR}, i_\alpha, i_{LER}) \quad (9)$$

The AM is utilized as a metric to assess how closely the printed pillars resemble an ideal cylindrical structure. Conversely, the GM can be employed to assess the overall suitability of the printed pillars for the desired application, by accounting for the multiplicative interaction of the sub-indexes. Notably, in scenarios where any of the desired characteristics deviates from the predefined target, it can significantly impact the final product, regardless of the values of other sub-indexes. Weights can be also assigned to individual sub- indexes in relation to the requirements of the final application. For instance, if the micropillars are intended for use as cell or biological interfaces, a rough surface texture and high AR are often desirable to promote cell adhesion and proliferation. In this case, the bending angle and diameter uniformity become less critical. Consequently, the two proposed PIs, Ψ_A and Ψ_G, provide a flexible and generalizable framework that can be tailored to meet diverse application-specific needs by adjusting the weights of the sub-indexes. The mathematical formulation of PIs are presented in Equations 10 and 11:

$$\Psi_A = AM\,(w_u \cdot i_u, w_{AR} \cdot i_{AR}, w_\alpha \cdot i_\alpha, w_{LER} \cdot i_{LER}),\ 0 \leq \Psi_A \leq 1 \quad (10)$$

$$\Psi_G = GM\,(w_u \cdot i_u, w_{AR} \cdot i_{AR}, w_\alpha \cdot i_\alpha, w_{LER} \cdot i_{LER}),\ 0 \leq \Psi_G \leq 1 \quad (11)$$

$$\text{with } \sum w_u, w_{AR}, w_\alpha, w_{LER} = 1$$

where $w_u, w_{AR}, w_\alpha, w_{LER}$ represent the weights associated with the respective sub-index. In this study, the equal weights of 0.25 were applied to all sub-indexes. Thus, under ideal circumstances (when $\Psi_A = \Psi_G = 0$), the printed pillar exhibits a minimal diameter variation along its height, a maximum AR, and an $\alpha = \frac{\pi}{2}$. Figure 2a illustrates the four sub-indexes as function of the geometrical metrics of the considered ideal shape.

For each AJ printed micropillar, the PIs were calculated and the most suitable printing parameters for HAR production were assessed. A least squares-based sparse parameterization model using LASSO regression technique was then trained on an extensive dataset: *CGF* = (20,25,30) sccm, with an *Rf* = (1,2,3,4). To ensure unbiased model evaluation, the DOE window (Table 1) was excluded from the training dataset and reserved for model validation. HAR micropillars were then AJ printed with the optimal parameters suggested by the model. Statistical analyses were conducted using the software Minitab® 2022.

4. Results and discussion

4.1. 3D AJ printed HAR micropillars

Figures 2b and 2c depict optical images of the 3D AJ printed HAR micropillars, from a lateral and a top view, respectively. It is visible that not all tested conditions successfully produced pillars, and their quality varies. An increase in *CGF* indeed leads to a decrease in both pillar quality and shape control, with a *CGF* = 40 sccm not resulting in pillars fabrication. Low *CGFs* enable the printing of pillars with their thickness decreasing as the *CGF* value is reduced from 30 to 20 sccm. Additionally, an *Rf* = 1 results in more defined pillars, and when an *Rf* = 3 pillars exhibit more surface irregularities and bending. The conditions at *CGF* = 40 sccm produced unacceptable results (Figure 2b) due to the high of material flow and were then excluded from the PIs calculation.

4.2. Printability Indexes

The calculated Ψ_A and Ψ_G confirm the previous visual observations, as reported in Table 2. Indeed, considering the sub-indexes ranges, the least impacting sub-index is i_α, followed by i_{AR}

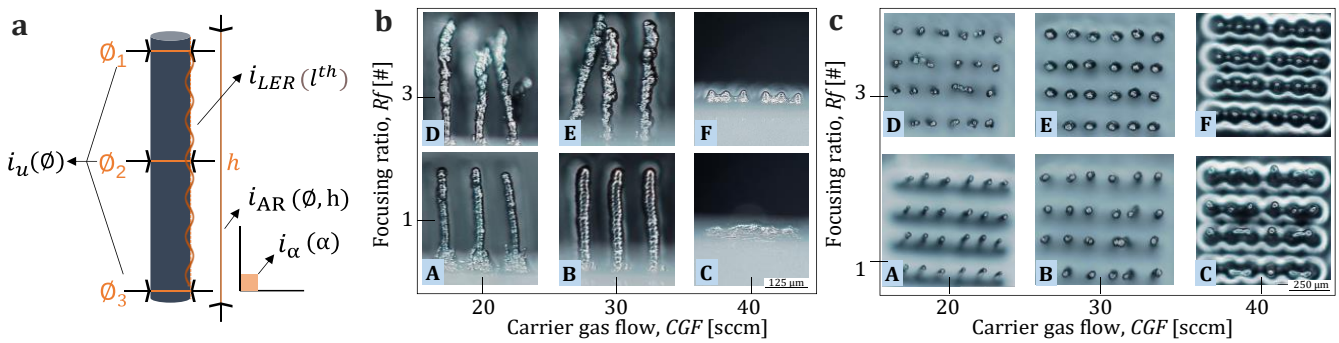

Figure 2. a) Representative image of the sub-indexes as function of geometrical metrics. Results of 3D AJ®P DOE window, with conditions labelled from A to F: b) lateral and c) top view.

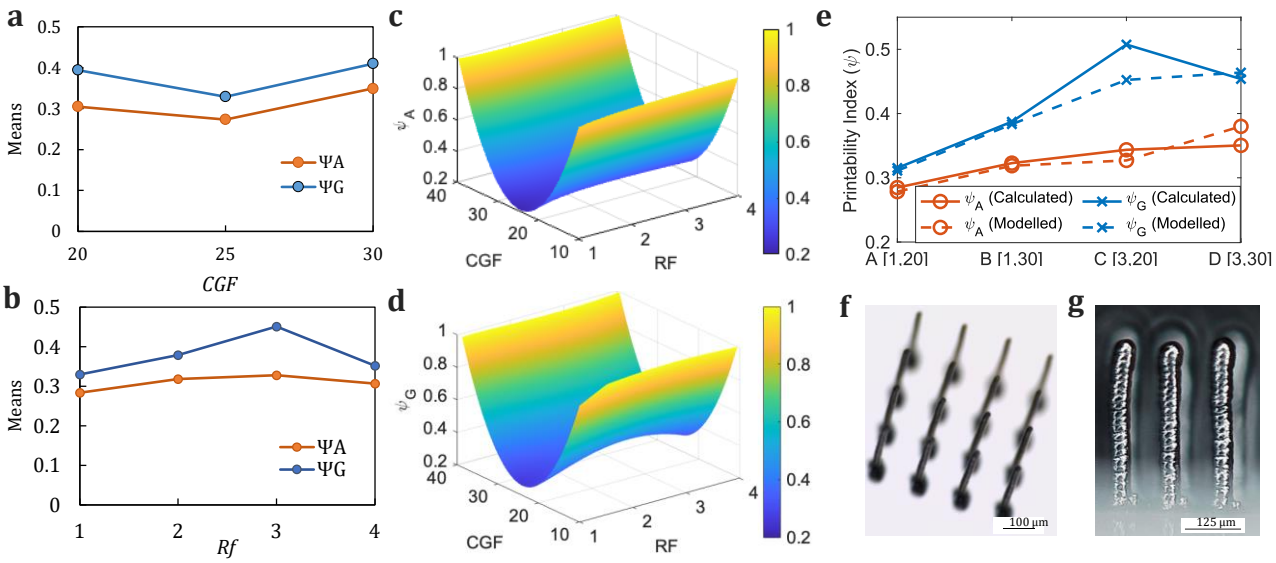

Figure 3. Main effects plots of Ψ_A and Ψ_G for the a) *CGF* and the *b) Rf*; Contour plots of model-based predicted PIs c) Ψ_A and d) Ψ_G; e) Comparison between the calculated PIs and the values predicted by the derived model, for the validation dataset; Optimal 3D AJ printed condition: f) array and g) pillars.

Table 2. Printability indexes for 3D AJ®P experimental design.

Condition	i_u	i_{AR}	i_α	i_{LER}	Ψ_A	Ψ_G
A	0.55 ± 0.0	0.10 ± 0.0	0.07 ± 0.0	0.42 ± 0.0	0.29 ± 0.0	0.32 ±0.0
B	0.28 ± 0.1	0.22 ± 0.0	0.06 ± 0.0	0.73 ± 0.1	0.31 ± 0.0	0.37 ±0.0
D	0.29 ± 0.0	0.15 ± 0.0	0.04 ± 0.0	0.89 ± 0.1	0.34 ± 0.0	0.51 ±0.0
E	0.29 ± 0.1	0.24 ± 0.0	0.05 ± 0.0	0.83 ± 0.0	0.35 ± 0.0	0.45 ±0.0
C, F	Not applicable					

and i_u, while i_{LER} has the greatest impact on the printability quality. Condition A (*Rf* = 1, *CGF* = 20 sccm) has the lowest, thus ideal, values for both Ψ_A and Ψ_G. Specifically, Ψ_G is always higher than Ψ_A, since is more influenced by sub-indexes variations. By using the extended dataset, Ψ_G remains still higher than Ψ_A, as depicted from Figures 3a and 3b in the main effects plots of *CGF* and *Rf* on Ψ_A and Ψ_G (normal distribution, P-value Ψ_A = 0.68, P-value Ψ_B = 0.62).

4.3. *Predictive Modelling and Validation for Process Optimization*

A sparse parametrized model, based on a LASSO regression technique, was then obtained for both Ψ_A and Ψ_G in order to related the PIs to the AJ®P process parameters. Model equations 12 and 13 are as follows:

$$\Psi_A = 0.28 + 0.01 \cdot \overline{Rf} - 0.5 \cdot \overline{CGF} - 0.04 \cdot \overline{\left(\frac{CGF}{Rf}\right)} + 0.54 \cdot \overline{CGF^2} - 0.05 \cdot \overline{CGF \cdot Rf} \quad (12)$$

$$\Psi_G = 0.34 + 0.4 \cdot \overline{Rf} - 0.55 \cdot \overline{CGF} + 0.05 \cdot \overline{\left(\frac{CGF}{Rf}\right)} + 0.53 \cdot \overline{CGF^2} - 0.35 \cdot \overline{Rf^2} \quad (13)$$

where, $\overline{feature}$ represents normalised $feature$ value. The derived models are used to predict the PIs Ψ_A and Ψ_G, as shown in Figures 3c and 3d, respectively. To evaluate the model's validity and performance, a comparative analysis was conducted between the calculated PIs derived from the dataset in Table 1 and the PIs predicted by the model, as reported in Figure 3e. The findings demonstrate a strong alignment between the calculated and model's predicted PIs, highlighting the robustness and accuracy of the proposed parameterisation approach. This is further supported by mean squared error (MSE) values of 0.0003 for Ψ_A and 0.0008 for Ψ_G. It also demonstrates its ability to obtain the relationship between the PIs and the process parameters. The model predicts a minimum value of PIs (Ψ_A = 0.212 and Ψ_G = 0.259) at the condition *Rf* = 1 with *CGF* = 24.4 sccm and *CGF* = 23.9 sccm, respectively. The predicted optimal parameters were validated experimentally through AJ®P (*Rf* = 1, *CGF* = 24 sccm). As shown in Figures 3f and 3g, the resulting 4x4 micropillar array is straight and well-aligned, confirming model's accuracy and applicability.

5. Conclusions and Outlook

This study proposes a printability assessment model for the quality manufacturing of HAR microstructures. Two variants of printability indexes are proposed. Both indexes are composed of four specifically designed quality sub-indexes derived from morphological imaging metrics, such as dimensional accuracy, overall shape fidelity and line edge quality. These metrics are shown to be the most flexible and accessible tools for evaluating quality of 3D HAR AJ printed micropillars.

The study then establishes a quantitative relationship between critical AJ®P process parameters (*i.e.*, *CGF* and *Rf*) and the PIs through a least squares-based sparse parameterization. The model effectively determines optimal process parameters for achieving the desired HAR geometry, as validated by experimental results. This enables a stable production and significantly reduces the trial-and-error time typical in the microfabrication of functional devices. The developed approach is a versatile model which can be exploited for different HAR shapes and technologies, expanding the framework to include additional sub-indexes and targeted application-specific dynamic weighting.

Future work will focus on refining more comprehensive PIs, enhancing the model reliability by collecting additional experimental data. Machine learning approaches will be finally integrated for in-built process control.

Acknowledgements

The authors acknowledge the Research Foundation Flanders (FWO) for the doctoral fellowship (1SB1120N) granted to Miriam Seiti and the MICS (Made in Italy – Circular and Sustainable) Extended Partnership (Next Generation EU (Italian PNRR – M4 C2, 1.3–D.D.1551.11-10-2022, PE00000004 CUP D73C22001250001).

References

[1]Zeis M., 2017, Deformation of thin graphite electrodes with high aspect ratio during sinking electrical discharge machining, *CIRP Annals*, 66(1):185–188.

[2]Takeuchi Y., Suzukawa H., Kawai T., et al., 2006, Creation of Ultra-precision Microstructures with High Aspect Ratios, *CIRP Annals*, 55(1):107–110.

[3]Oehrlein G.S., Brandstadter S.M., Bruce R.L., et al., 2024, Future of plasma etching for microelectronics: Challenges and opportunities, *Journal of Vacuum Science and Technology B*, 42(4):041501.

[4]Lucchetta G., Sorgato M., Carmignato S., and Savio E., 2014, Investigating the technological limits of micro-injection molding in replicating high aspect ratio micro-structured surfaces, *CIRP Annals*, 63(1):521–524.

[5]Gerami A., Alzahid A.Y., Mostaghimi P., et al., 2019, Microfluidics for Porous Systems: Fabrication, Microscopy and Applications, *Transport in porous Media, Springer*, 130:277–304.

[6]Kamranikia K., Dominici S., Keller M. et al., 2023, Very High-Aspect-Ratio Polymeric Micropillars Made by Two-Photon Polymerization, *Micromachines*, 14(8), 1602.

[7]Krieger K.J., Bertollo N., Dangol M., 2019, Simple and customizable method for fabrication of high-aspect ratio microneedle molds using low-cost 3D printing, *Microsystems & Nanoengineering*, 5(42).

[8]Bucciarelli A., Paolelli X., De Vitis E., 2022, VAT photopolymerization 3D printing optimization of high aspect ratio structures for additive manufacturing of chips towards biomedical applications, *Additive Manufacturing*, 60:103200.

[9]Zips S., Huang B., Hotte S. et al., 2023 Aerosol Jet-Printed High-Aspect Ratio Micro-Needle Electrode Arrays Applied for Human Cerebral Organoids and 3D Neurospheroid Networks, *ACS Applied Material Interfaces*, 15(30):35950–35961.

[10]Ramesh S., Mahajan C., Gerdes S. et al., 2022, Numerical and Experimental Investigation of Aerosol Jet Printing, *Additive Manufacturing*, 59:103090.

[11]Takaya Y., Michihata M., Hayashi T. et al., 2012, Dimensional measurement of microform with high aspect ratio using an optically controlled particle with standing wave scale sensing, *Cirp Annals*, 61(1):479-482.

[12]Schwab A., Levato R., D'Este M. et al., 2020, Printability and Shape Fidelity of Bioinks in 3D Bioprinting, *Chemical Reviews*, 120(19):11028-11055.

[13] Ketel S., Falzone G., Wang B., Washburn N., Sant G., 2019, A printability index for linking slurry rheology to the geometrical attributes of 3D-printed components', *Cement and Concrete Composites*, 101(32–43).

[14]Seiti M., Degryse O., Ferraro R.M. et al., 2023, 3D Aerosol Jet® printing for microstructuring: Advantages and Limitations, *International Journal of Bioprinting*, 9(6):57–74.

[15] Constantoudis V., Patsis G.P., Leunissen L.H.A., et al., 2004, Line edge roughness and critical dimension variation: Fractal characterization and comparison using model functions, *Journal of Vacuum Science and Technology B*; 22 (4): 1974–1981.